



Title	Upper mantle structure of marginal seas and subduction zones in northeastern Eurasia from Rayleigh wave tomography
Author(s)	Bourova, E.; Yoshizawa, K.; Yomogida, K.
Citation	Physics of the Earth and Planetary Interiors, 183(1-2), 20-32 <a href="https://doi.org/10.1016/j.pepi.2010.06.007">https://doi.org/10.1016/j.pepi.2010.06.007</a>
Issue Date	2010-11
Doc URL	<a href="http://hdl.handle.net/2115/44907">http://hdl.handle.net/2115/44907</a>
Type	article (author version)
File Information	PEPI183-1-2_20-32.pdf



[Instructions for use](#)

# Upper mantle structure of marginal seas and subduction zones in Northeastern Eurasia from Rayleigh wave tomography

E. Bourova<sup>a,b,\*</sup>, K. Yoshizawa<sup>a,c</sup>, K. Yomogida<sup>a</sup>

<sup>a</sup>*Earth and Planetary Dynamics, Faculty of Science, Hokkaido University, Sapporo 060-0810, Japan*

<sup>b</sup>*Laboratoire de Geophysique Interne et Tectonophysique, 1381 rue de la Piscine, 38400 Saint Martin d'Herès, France*

<sup>c</sup>*Lamont-Doherty Earth Observatory, Columbia University, Palisades, NY 10964, USA*

---

## Abstract

The upper mantle structure of marginal seas (the Seas of Japan and Okhotsk) and subduction zones in northeastern Eurasia is investigated, using the three-stage multimode surface wave tomography incorporating finite-frequency effects. Broadband waveform data from 305 events with magnitude greater than 5.5 from 1990 to 2005 recorded at 25 stations of the IRIS network in northeastern Eurasia and Japan and at 8 stations of the broadband seismic network in Far Eastern Russia from 2005 to 2008 are employed in our analysis. The dispersion curves of the fundamental mode and first two higher modes of Rayleigh waves are simultaneously inverted for the shear-wave velocity structure of the region. The off-great circle propagation due to strong heterogeneities in the region is also taken into account in the construction of intermediary phase velocity models for each mode as a function of frequency. The obtained 3D S-wave velocity model is well re-

---

\*Corresponding author

*Email address:* [katia.bourova@obs.ujf-grenoble.fr](mailto:katia.bourova@obs.ujf-grenoble.fr) (E. Bourova)

solved down to 200 km depth. Checkerboard tests show the average horizontal resolution of 5 degrees in the study region. The subducting Pacific plate is clearly imaged as a high velocity anomaly up to 6 percents. The mantle wedge above the Pacific plate is associated with low velocity anomalies. The absolute minimum S wave velocity in the mantle wedge is 4 km/s in the Sea of Okhotsk in the depth range from 80 to 160 km, probably indicating the presence of partial melt. The anomalous spot with conspicuous low velocity in the southern end of the Sea of Okhotsk may indicate the existence of hot upwelling flow in the mantle. A high velocity anomaly subparallel to the present subduction zone is found in the north-western Sea of Okhotsk in the depth range from 100 to 200 km. The position of this anomaly correlates well with the high velocity anomaly found in the P-wave tomography of Gorbatov et al. (2000), which may be interpreted as a relict of the Okhotsk plate subducted in the past. We also attempted a mapping of azimuthal anisotropy in this region. The fast phase velocity directions near the Pacific plate are observed subparallel to the Kuril and Japan Trenches at all the periods, indicating a strong effect of the subducting Pacific plate on the mantle flow, while the anisotropy appears to be weak in tectonically inactive marginal seas.

*Keywords:* Rayleigh waves, S wave velocity, upper mantle structure, the Sea of Japan, the Sea of Okhotsk.

---

## 1. Introduction

2 The Seas of Japan and Okhotsk are marginal seas in northeastern Eurasia, and  
3 their associated subduction zones are characterized by complex tectonic struc-  
4 ture and geologic history. Located at junctions of six major plates (Bird, 2003),  
5 the northeastern Eurasian region confines several subduction zones, arc-arc junc-

6 tions and back-arc basins (see Figure 1). In north-eastern Japan, the Pacific plate  
7 subducts beneath the Okhotsk plate at a rate of about 8-10 cm/year to the west-  
8 northwest (Hasegawa et al., 1994; Bird, 2003). This subduction process is related  
9 to high volcanic activities in this area. In south-western Japan, the Philippine Sea  
10 plate subducts to the northwest beneath the Amur plate at a rate of 4.5 cm/year  
11 (Sugimura, 1972; Ando, 1975; Seno et al., 1993). The eastern end of the Philip-  
12 pine Sea plate subducts beneath the Okhotsk plate to the north. The Okhotsk plate  
13 is regarded as a plate independent of the major North-American plate (Seno et al.,  
14 1996). The Amur plate moves slowly with respect to the Eurasian plate (Zonen-  
15 shain and Savostin, 1981; Wei and Seno, 1998), colliding with the Okhotsk plate  
16 (Seno, 1999).

17     Origin and tectonic evolution of the present marginal seas in this area are  
18 highly complex, and details of their tectonic history have not been well resolved  
19 due to the lack of extensive surveys in the seas. While the formation of the  
20 Japanese Islands is closely related to the opening of the Sea of Japan, their de-  
21 tail evolution is grossly estimated by some surveys of geomagnetic anomalies in  
22 the Sea of Japan as well as paleomagnetic studies of basement rocks in the islands  
23 (Taira, 2001). The information of the Sea of Okhotsk is further limited with a  
24 few geomagnetic surveys available (Verzhbitsky et al., 2006). Verzhbitsky and  
25 Kononov (2006) proposed an evolution model of the Sea of Okhotsk over the past  
26 90 Ma.

27     The tectonics in the northeastern Eurasia region is governed primarily by the  
28 oceanic Pacific plate subducting beneath the Okhotsk and Philippine Sea plates  
29 along Kamchatka, Kuril, Japan and Izu-Bonin seismogenic zones. The seismicity  
30 beneath the Japan trench represents a deep seismic zone in the Pacific plate dip-

31 ping at an angle of 30 degrees or more. Intermediate and deep earthquakes occur  
32 down to a depth of about 670 km. The intermediate seismicity around 60-200 km  
33 depth is splitted into two planar groups, parallel to each other and 30-40 km apart,  
34 called a double seismic zone (Hasegawa et al., 1978, 1991; Zhao et al., 2009).  
35 The dip angle of the subducting slab beneath the Kuril trench is slightly higher  
36 than that of the Japan trench, ranging from 40° to 55° (Castle and Creager, 1998;  
37 Hasegawa et al., 1994; Katsumata et al., 2003).

38 Beneath the Kamchatka peninsula, the Pacific plate subducts westward at a  
39 rate of about 8 cm/year, according to NUVEL-1 (DeMets et al., 1990; DeMets,  
40 1992). In the southern part of the Kamchatka, a Wadati-Benioff zone defines a  
41 downgoing slab to the maximum depth of 500 km, dipping at an angle of about  
42 55°. Near the Aleutian-Kamchatka corner, this depth shallows gradually to 300  
43 km and the dip angle of a Wadati-Benioff zone decreases from 55° to 35° (Gorbatov  
44 et al., 1997; Park et al., 2002).

45 Investigation of the 3D mantle structure in this region should enable us to  
46 better understand its complex tectonic processes. In the last two decades, seis-  
47 mic tomography methods have been intensively applied to the mantle structure in  
48 northeastern Eurasia and Japan on global and regional scales. Many researchers  
49 used body wave tomography techniques to obtain images of the Pacific plate sub-  
50 ducting beneath this region (van der Hilst et al., 1991, 1998; Widiyantoro et al.,  
51 1999; Gorbatov et al., 2000; Zhao, 2001, 2004; Miller et al., 2006; Huang and  
52 Zhao, 2006; Zhao, 2009). The Pacific plate has been imaged down to 660 km  
53 depth, where it stagnates near the mantle transition zone (Fukao et al., 2001).

54 In addition, high resolution images of the mantle beneath the Japanese islands  
55 have been obtained by body wave tomography with a high velocity Pacific plate

56 introduced into initial models (Hasegawa et al., 1991; Zhao et al., 1994; Mishra  
57 et al., 2003; Wang and Zhao, 2005; Shelly et al., 2006; Zhao et al., 2009). This  
58 technique allows us to map small-scale heterogeneities in the region successfully,  
59 although such results depend on the validity of the initial assumption. The ob-  
60 tained models show a sharp P-wave velocity contrast across the top of the Pacific  
61 slab, and small-scale low velocity anomalies are imaged beneath several active  
62 volcanoes.

63 On the other hand, the resolution of body wave tomography on both local  
64 and global scales is limited beneath the Seas of Japan and Okhotsk because of  
65 a non-uniform distribution of earthquakes and a lack of seismic stations there.  
66 The 3D upper mantle structure of this region may be better constrained by surface  
67 waves, but only a few studies with local-scale surface wave tomography have been  
68 ever performed (Li et al., 2001; Lebedev and Nolet, 2003; Takezoe et al., 2005).  
69 These studies covered only the Japanese islands and the Sea of Japan. Most of  
70 the Seas of Japan and Okhotsk have been investigated only as a part of large-scale  
71 surface wave tomography studies (van Heijst and Woodhouse, 1999; Ritzwoller  
72 and Levshin, 1998; Priestley et al., 2006).

73 In this study, we present a three-dimensional S-wave velocity model of the up-  
74 per mantle beneath the Seas of Japan and Okhotsk and their neighbouring region  
75 in Northeastern Eurasia with Rayleigh waves. Subduction zones are known as a  
76 region of strong heterogeneities, resulting in large off-great circle propagations,  
77 for example, in the northwestern Pacific ocean (Isse et al., 2006). In such circum-  
78 stances, velocity structures are not properly modelled by the conventional surface  
79 wave ray theory. We therefore use the method of multimode surface wave tomog-  
80 raphy of Yoshizawa and Kennett (2004), which allows us to take into account both

81 ray bendings and finite-frequency effects. The vertical resolution is enhanced by  
82 the simultaneous use of the fundamental and first two higher modes of Rayleigh  
83 waves. We also analyze azimuthal variations of phase velocity as the first attempt  
84 to retrieve local-scale anisotropic characters in this region.

## 85 **2. Data and Method**

86 In this study, we used three-component broad-band seismograms of FARM  
87 (Fast Archive Recovery Method) data collected from the IRIS (Incorporated Re-  
88 search Institutions for Seismology) network in the Northeastern Eurasian region  
89 (30°N-75°N latitude, 120°E-175°E longitude). The IRIS station distribution in  
90 this region is, however, too sparse to fully constrain the regional structure around  
91 the Seas of Japan and Okhotsk. As a part of Japanese Stagnant Slab Project for de-  
92 lineating stagnant slabs in the mantle transition zone beneath Northeastern Eura-  
93 sia, a temporary seismic network with 8 broadband stations has been deployed in  
94 Far Eastern Russia since 2004 (Miyamachi et al., 2009). We included the data  
95 from this regional network to improve the horizontal resolution of our results and  
96 to better understand the dynamics processes occurring in the region.

97 We selected seismic events of magnitude greater than 5.5  $M_w$  from 1990 to  
98 2005 for the IRIS data, and from September 2005 to December 2008 for the  
99 temporary Far-East Russian stations. We chose Rayleigh waveforms with good  
100 signal-to-noise ratio recorded in the vertical component of the seismograms. The  
101 used data set is composed of 33 stations and 305 events. The distributions of  
102 stations and events are shown in Figure 2. Locations and origin times of the earth-  
103 quakes are taken from the IRIS catalogue. The centroid moment tensor solutions  
104 from the global CMT catalogue (Ekström et al., 2005) are used. All the data are

105 initially corrected with an instrument response of each station.

106 The obtained waveforms are processed by the three-stage inversion technique  
107 proposed and developed by Kennett and Yoshizawa (2002) and Yoshizawa and  
108 Kennett (2004), which comprises the following three independent steps:

109 (1) We extract the dispersion information of each available source-station path  
110 from the observed waveform. The phase velocity dispersion curve is mea-  
111 sured for the fundamental and first a few higher modes through waveform  
112 fitting.

113 (2) The dispersion information from all the paths is combined to produce mul-  
114 timode phase velocity maps as a function of frequency. Linear inversions  
115 are performed based on the assumption that the surface wave paths follow  
116 great-circles. Subsequently, 2-D phase velocity maps are updated by in-  
117 cluding ray traces and finite-frequency effects.

118 (3) We invert the local dispersion information at each location point for a lo-  
119 cal one-dimensional S-wave velocity profile. The final three-dimensional S  
120 wave velocity model is constructed from the set of the updated multimode  
121 phase velocity maps.

122 This approach offers the advantage of combining a variety of information such as  
123 multi-mode dispersion, off-great circle propagation and finite-frequency effects in  
124 a common framework.

### 125 **3. Path averaged multimode dispersion curves**

126 To retrieve the multimode dispersion information for each path in the first  
127 step of the three-stage inversion, we used the fully non-linear waveform inversion  
128 method of Yoshizawa and Kennett (2002a) based on the neighbourhood algorithm



129 (NA) of Sambridge (1999). The NA is used as a global optimizer to find models  
130 with smaller misfit in a model parameter space. Filtered seismograms in different  
131 frequency ranges and their weighted envelopes are simultaneously minimized.

132 In this waveform inversion, a set of path averaged one-dimensional S-wave  
133 velocity models are generated through the non-linear waveform fitting with the  
134 NA for each event-station path. We calculated 3000 S-wave velocity models for  
135 each path. The best fit model corresponding to the minimum of the misfit function  
136 is selected to estimate the multi-mode dispersion. The standard error is estimated  
137 as a standard deviation from the best 1000 models. Then, the reliability parameter  
138 defined by Yoshizawa and Kennett (2002a) is calculated for the best fit model,  
139 which quantifies the relative amplitudes of each mode excited at the source as  
140 well as the degree of fit between synthetic and observed waveforms.

141 As a reference model to initiate this model parameter search, we used PREM  
142 (Dziewonski and Anderson, 1981) or PREMC (a modified version of PREM to  
143 better represent the continental upper mantle), depending on a path whether it lies  
144 mostly on an oceanic or a continental region. The crustal structure is corrected  
145 beforehand using the 3SMAC model (Nataf and Ricard, 1996).

146 We restricted the analyzed period range to be longer than 30 seconds to avoid  
147 unwanted effects of mode branch coupling (Kennett, 1995). We only used the data  
148 from relatively far events with angular distances greater than 9 degrees (or about  
149 1000 km), so that the fundamental-mode Rayleigh waves are reasonably separated  
150 from their preceding body wave arrivals.

151 In order to check the quality of the measured dispersion curves, we applied  
152 a manual quality control for the IRIS-FARM data set according to several data  
153 selection criteria. First, we discard seismograms if the station is located in a nodal

154 direction from the source for the radial amplitude of Rayleigh waves roughly less  
155 than a half of the maximum. Next, we perform the inversion with five different  
156 initial models, from “Model 1” to “Model 5”, which includes S-wave velocity  
157 perturbations of -3 to +3% from a reference model in the top 250 km with 1.5%  
158 increment. We only keep the data which provide stable waveform inversion results  
159 for all the models, and the resultant dispersion curves are checked visually to  
160 discard some outliers. The threshold values for the minimum reliability parameter  
161 is set to 4 for the fundamental mode and 1.5 for the first higher mode. If all the  
162 criteria mentioned above are acceptable, the data are selected for the second stage  
163 of the inversion scheme.

164 An example of the NA waveform inversion for IRIS-FARM data is illustrated  
165 in Figure 3 for an earthquake of magnitude  $M_w=6.1$  near the eastern coast of  
166 Honshu (Japan) on 3rd October 2000 recorded at the station HIA. Using “Model  
167 3” as the initial model in this example, we display the best-fit waveforms (Figure  
168 3a), the best fit path averaged S-wave velocity model (Figure 3b), the multimode  
169 phase velocity dispersion curve (Figure 3c) and the reliability parameter (Figure  
170 3d).

171 For the data set from the network in Far East Russia, we used a new automated  
172 method developed by Yoshizawa and Ekström (2009). The quality of waveform fit  
173 and phase speed measurements are checked through several quantitative param-  
174 eters with empirical threshold criteria, including an average radiation amplitude  
175 of each mode, a total misfit of multiple time windows, and a reliability paramete-  
176 ter. The combination of these parameters enables us to select reliable dispersion  
177 measurements in a fully automatic manner.

178 We measured phase velocity dispersion curves from 30 to 150 s period for the

179 fundamental mode, from 30 to 140 s for the first higher mode and from 30 to 120  
180 s for the second. The number of the used paths depends on period and varies from  
181 980 to 1099 with a total of 1129 different paths. The distribution of the selected  
182 paths is shown in Figure 4.

#### 183 **4. Multimode phase velocity dispersion curves**

184 In the second stage, the dispersion curves obtained for various paths are used  
185 to reconstruct phase velocity maps of the region. Following Yoshizawa and Ken-  
186 nett (2004) we obtain two types of phase velocity models, called GC and Riz  
187 models, which are derived from different assumptions. First, we calculate period-  
188 dependent phase velocity maps, GC models, supposing that surface waves propa-  
189 gate along great circles. These models use the great circle approximation without  
190 any consideration of the off-great circle propagation and of the zone of influence.  
191 Phase velocity maps are calculated at periods from 30 to 150 s for the funda-  
192 mental and first two higher modes of Rayleigh waves with a grid interval of 3.0  
193 degrees. Figure 5a shows an example of the GC models for the fundamental mode  
194 of Rayleigh wave at period of 50 s.

195 We then obtain an updated phase velocity maps, Riz models, using ray tracing  
196 in the reference heterogeneous models, GC models, derived from the great-circle  
197 approximation. In this updating process, we also consider finite frequency effects  
198 using an influence zone, in which surface waves are coherent in phase (Yoshizawa  
199 and Kennett, 2002b). To expand the phase velocity perturbation over the influ-  
200 ence zone, we use a spherical B spline function (Lancaster and Salkauskas, 1986;  
201 Wang and Dahlen, 1995) defined at the center of a geographical cell as a basis  
202 function. The detailed inversion method for phase velocity models is described

203 by Yoshizawa and Kennett (2002a). The Riz models (Figure 5b), improve results  
204 of the phase velocity mapping in a similar manner to previous studies (e.g. Isse et  
205 al., 2006).

206 The trade-off between the model norm and the resolution in model for this  
207 inversion is controlled by an arbitrary damping parameter  $\lambda$ . Figure 6 shows the  
208 trade-off curve for the Riz model of the fundamental mode at period of 100 s,  
209 very similar to that for the corresponding GC model. As reasonable compromise  
210 between the misfit and the model norm, we chose the damping parameter  $\lambda =$   
211 1.0 in this example. The highest variance reduction of 54% is achieved for the  
212 fundamental mode at period of 50 s for the Riz model, and from 23% to 49%,  
213 depending on period, for the first and second higher modes.

214 To estimate the horizontal resolution of the present inversion, we performed  
215 checkerboard tests at period of 50 s with anomalies of  $\pm 4.8$ -percent amplitude  
216 for 4, 5, 6 and 8 degree cell sizes (Figure 7), considering the effects of off-great  
217 circle propagation and finite frequency of surface waves for both forward and in-  
218 verse modellings. These tests show that the available path coverage provides us  
219 with good resolution beneath the Seas of Japan and Okhotsk for anomalies of 5  
220 degrees and more, while small-scale anomalies of 4 degrees cannot be resolved  
221 sufficiently. To preserve the resolved features, we adopted a model with 3 degrees  
222 of distance between the grid points. Nevertheless, some small anomalies could  
223 be artefacts in such model due to the gridding. While using the 3 grid model,  
224 we avoid discussions on small-scale anomalies less than 5 degrees in the inter-  
225 pretation of our results. The influence of different grid sizes on our final S-wave  
226 velocity model is discussed in section 5.1.

227 Figures 8 shows the resulting phase velocity maps of fundamental-mode Rayleigh

228 waves at periods of 50, 75, 100 and 150 s with grids of 3 degrees. A large-scale  
 229 high velocity anomaly can be seen in all the maps along the Kuril and Japan  
 230 trenches which corresponds to the subducting Pacific slab. Low velocity anoma-  
 231 lies beneath the east of the Sea of Japan and the southeast of the Sea of Okhotsk  
 232 are associated with the mantle wedge above the subducting slab where we would  
 233 expect high temperature anomalies.

## 234 **5. Three-dimensional S-wave velocity model**

### 235 *5.1. Inversion for S-velocity model*

236 In the final stage, the local dispersion curves are inverted into a one-dimensional  
 237 S wave velocity model at each point of the region. The inverted one-dimensional  
 238 models are then assembled into the final three-dimensional S wave velocity map.  
 239 The relation of multimode phase dispersion and local one-dimensional structure  
 240 can be represented by the following linearized relation (Takeuchi and Sato, 1972;  
 241 Dahlen and Tromp, 1998):

$$\frac{\delta c(\omega)}{c} = \int_0^R \left\{ K_\rho(\omega, z) \frac{\delta \rho(z)}{\rho} + K_\alpha(\omega, z) \frac{\delta \alpha(z)}{\alpha} + K_\beta(\omega, z) \frac{\delta \beta(z)}{\beta} \right\} dz, \quad (1)$$

242 where  $\delta c$  is the perturbation of phase velocity in frequency or period;  $\delta \rho$ ,  $\delta \alpha$  and  $\delta \beta$   
 243 are the perturbations of density, P-wave velocity and S-wave velocity as a function  
 244 of depth, respectively; and  $R$  is the maximum depth considered. The sensitivity  
 245 kernels  $K_\rho$ ,  $K_\alpha$  and  $K_\beta$  represent the partial derivatives of phase velocity with  
 246 respect to each of the model parameters. Since the phase velocity of surface waves  
 247 is mostly sensitive to S-wave velocity structure with only limited sensitivity to P-  
 248 wave velocity and density perturbations (Nataf et al., 1986), we fix the density

249 and P velocity structures to a reference model and invert only for S-wave velocity  
250 perturbations.

251 Both the fundamental mode and the first two higher modes of Rayleigh waves  
252 are inverted simultaneously by the iterative least squares inversion scheme of  
253 Tarantola and Valette (1982). The smoothness of the resulting one-dimensional  
254 model is represented by a priori model covariance with a Gaussian distribution  
255 (Cara and L ev eque, 1987; Nishimura and Forsyth, 1989). The degree of smooth-  
256 ness is parametrized by a correlation length  $L$  and a standard deviation  $\sigma$ . We used  
257  $\sigma = 0.1$  km/s and  $L = 20$  km beneath the Moho. Above the Moho, the correlation  
258 length is chosen to be  $L = 5$  km with the same  $\sigma$  to allow more rapid velocity  
259 variations.

260 The one-dimensional models obtained by the above inversion generally de-  
261 pend on the adopted initial model. Since the average phase velocity measured in  
262 our study region is significantly lower than PREM, we used “PREM-3%” as the  
263 initial model with 3 percents slower than PREM in the upper mantle. In addi-  
264 tion, the initial model is adapted to have smooth variations across boundaries at  
265 220, 400 and 670 km depth and its crustal part is corrected by the 3SMAC model  
266 (Nataf and Ricard, 1996), similar to the case of the first stage.

267 The resolution kernels with S-wave velocity for a typical one-dimensional  
268 model are presented in Figure 9 for the location of (35N, 140E). These profiles  
269 show comparatively good resolution down to the depth of 200 km where the struc-  
270 ture is mainly constrained by the fundamental mode. The higher modes are less  
271 sensitive to S-wave velocity variations compared to the fundamental mode, so that  
272 the resolution is not satisfactory at the depth below 200 km. Nevertheless, there is  
273 some sensitivity down to 250 km depth, mostly owing to the higher modes.

274 Figure 10 displays four models of S wave velocity perturbations at 100 km  
275 depth obtained for different grid sizes: 2, 3, 4 and 5 degrees. The distribution of  
276 S-wave velocity is plotted relative to the average S-wave velocity at each depth.  
277 The 2 degree model contains some small-scale anomalous patches, which could  
278 be artefacts due to poor horizontal resolution. In contrast, the 5 degree model  
279 presents a reliable but much smoother solution of the inversion. In the subsequent  
280 discussion, we use the 3-degree model with a reasonably good resolution in the  
281 entire region.

### 282 *5.2. 3D model of the northeastern Eurasian region*

283 Horizontal depth slices of S wave velocity are presented for the final three-  
284 dimensional model in the depth range from 50 to 200 km in Figure 11. The  
285 southwest part of the Japanese islands (30-35 degree latitude) is excluded from  
286 our result because the number of ray paths in this region is rather small (see Fig-  
287 ure 4) and the model is less reliable. The overall S-velocity structure in this region  
288 is dominated by a high velocity anomaly associated with the subduction of the Pa-  
289 cific plate. The subducting Pacific plate shows conspicuous velocity contrast with  
290 the surrounding mantle up to 6% at depth shallower than 200 km.

291 Beneath the Sea of Okhotsk, the depth slice at 50 km presents a relatively  
292 high velocity anomaly of 3% in the southern part of the Sea of Okhotsk. This  
293 anomaly correlates well with the position of the South Kuril Basin (or the South  
294 Okhotsk basin) underlain by oceanic lithosphere (see Figure 4 of Verzhbitsky et  
295 al., 2006). In contrast, there are no significant velocity anomalies in the northern  
296 part, which corresponds to Central Okhotsk massif with continental crust. The  
297 Kamtchatka Peninsula shows low velocity at depth of 50 km, implying active  
298 tectonic activities of an island arc type with thick continental crust. The S-velocity

299 maps at depth of 100-200 km display the presence of noticeable low velocity  
300 anomalies in the southeastern Sea of Okhotsk along the Kuril subduction zone.  
301 In this area, negative velocity perturbations reaches about -10 %. We show three  
302 vertical cross sections of the 3D S-wave velocity model in Figure 12. The profiles  
303 are nearly perpendicular to each section of the subduction zone. Two of them are  
304 close to the profiles published in previous studies: AA' corresponding to the cross-  
305 sections AA' of Lebedev and Nolet (2003), and the cross-section CC' comparable  
306 to DD' or EE' of Gorbatov et al. (2000).

307 The cross-sections AA', BB' and CC' show the S-wave velocity perturbations  
308 beneath the northern Japan and the Sea Okhotsk down to 250 km depth. The  
309 subducting Pacific plate is well resolved as a high velocity anomaly of approxi-  
310 mately 6 percents. The limited lateral resolution of our data does not allow us to  
311 resolve the precise shape of the slab, resulting that the imaged slab appears more  
312 elongated and flatter than the actual plate.

313 In the central part of the cross-section BB', beneath the southern Sea of Okhotsk,  
314 we find a large low velocity anomaly. The absolute S-wave velocities are as low  
315 as 4.0 km/s at depth of 80-160 km, indicating the presence of partial melt. The  
316 overall stress field in the Hokkaido region has been found anomalous, not con-  
317 sistent with the stress field predicted by the subductions of its surrounding major  
318 plates of Figure 1. The strong low velocity anomalous spot in the southern end  
319 of the Sea at depth of 80 to 160 km may support a hypothesis of hot upwelling  
320 flow in the mantle in the south of the Sea of Okhotsk, although there have been no  
321 direct observational evidences.

322 Another interesting feature is a high velocity anomaly in the north-western  
323 Sea of Okhotsk (in the left of cross sections BB' and CC') found between 100 and



324 250 km depth. The lateral size of the anomaly is at least 500 km. The anomaly  
325 is extended in the NE-SW direction, subparallel to the present Pacific subduction  
326 zone. The S-wave velocity perturbation of this anomaly is approximately +6 per-  
327 cents, nearly the same as obtained for the Pacific slab. The position and amplitude  
328 of this high velocity anomaly seems to indicate an extinct subduction zone behind  
329 the Kuril trench.

330 A high velocity anomaly in P wave was imaged by Gorbatov et al. (2000), sub-  
331 parallel to the Pacific subduction zone in the northern part of the Sea of Okhotsk,  
332 between 200 and 660 km depth. They suggested that it may correspond to the  
333 relict of the subducted Okhotsk plate. The Okhotsk subduction zone was once ac-  
334 tive before ~55 Ma. The cessation of the subduction process seems to be caused  
335 by the trapping of the Okhotsk plate after a jump in the subduction zone from the  
336 northern Asian margin to the Kuril-Kamchatka trench, which is estimated to have  
337 occurred in the period of 55-65 Ma (Parfenov and Natal'in, 1985; Kimura, 1994).  
338 Taking advantage of better resolution of the surface waves in the Sea of Okhotsk,  
339 we confirm the presence of the above high velocity anomaly beneath the northern  
340 part in the depth range of 100-200 km, consistent with the result of Gorbatov et  
341 al. (2000).

342 There are other anomalous parts in the 3-D S wave velocity model than those  
343 beneath the Sea of Okhotsk. The northern Sea of Japan (Japan Basin in Figure 1)  
344 is characterized by slightly high velocity anomaly shallower than 100 km and low  
345 in a deeper range, implying its lithosphere to be oceanic. The depth slice at 50 km  
346 in Figure 11 shows slightly high velocities in Japan Basin in comparison with the  
347 other parts of the Sea, which can be explained by the presence of different types of  
348 oceanic lithosphere within the Sea. However, we have only the limited azimuthal

349 coverage of ray paths in this area (Figure 4), so that its horizontal resolution is as  
350 large as about 5 degrees (Figure 7). Therefore, we are not able to give decisive  
351 conclusions on small-scale variations of S-wave velocities in this region from the  
352 current model. A more detailed structure in this region has recently been inves-  
353 tigated by Yoshizawa et al. (2010) with higher resolution. They imply that its  
354 shallow structure is likely to be different from the standard oceanic lithosphere.

355 The S-wave velocity model includes several anomalous areas beneath the north-  
356 eastern corner of the Eurasian continent although they are not highly reliable due  
357 to sparse path coverage and poor resolution in this part of our model. A low  
358 anomalous spot exists near the triple border of Russia, China and North Korea,  
359 particularly in a depth range from 100 to 150 km, as shown in Figure 11 and AA'  
360 of Figure 12. Lei and Zhao (2005) proposed a region of low velocity anomaly be-  
361 neath the historically active Changbai (Baekdu) volcano with their P-wave travel  
362 time tomography. Lei and Zhao (2005) interpreted this low velocity anomaly as  
363 an intraplate volcano associated with the deep subduction of the Pacific slab. For  
364 details, please also refer to Zhao et al. (2009). Our low velocity anomaly may  
365 correspond to this proposed intraplate volcano although its location is slightly dif-  
366 ferent, probably due to the poor resolution of the current model in this area.

367 A slow velocity anomaly is found in the depth below 150 km in the south of  
368 Hokkaido, but this location is close to an edge of our model space. Therefore, we  
369 are unable to discuss the detailed local structure in this area.

## 370 **6. Azimuthal anisotropy around the Japanese islands**

371 Using path-specific phase velocities, we estimate dominant features of az-  
372 imuthal anisotropy for the fundamental-mode Rayleigh wave, which would pro-

373 vide us with useful information on the mantle dynamics beneath this region that  
374 cannot readily be inferred from the isotropic S-wave velocity model. The az-  
375 imuthal anisotropy of surface waves can be modelled by the following linear ap-  
376 proximated formulation (Backus, 1965; Smith and Dahlen, 1973) under the as-  
377 sumption of weak anisotropy:

$$c(\mathbf{r}, \psi) = c_0(\mathbf{r}) + A_1(\mathbf{r}) \cos 2\psi + A_2(\mathbf{r}) \sin 2\psi + A_3(\mathbf{r}) \cos 4\psi + A_4(\mathbf{r}) \sin 4\psi, \quad (2)$$

378 where  $\mathbf{r}$  is the position vector on a sphere,  $\psi$  is the direction of wave propagation,  
379  $c_0$  is the isotropic part of phase velocity, and  $A_i$  are the anisotropic coefficients.  
380 As can be understood from equation (2), introducing the azimuthal anisotropy  
381 dramatically increases the number of parameters to be determined and the rela-  
382 tively uniform azimuthal distribution of ray paths is required. Figure 13 shows  
383 a checkerboard resolution test for azimuthal anisotropy at period of 50 s for 8  
384 and 10-degree cellular patterns. This resolution test suggests that our data set is  
385 sufficient to retrieve large-scale patterns of azimuthal anisotropy. For simplicity,  
386 we use the great-circle approximation without any effect of finite frequency in the  
387 inversion for azimuthal anisotropy. The inversion is performed only for isotropic  
388 term  $c_0$  and  $2\psi$  terms ( $A_1$  and  $A_2$ ), and  $4\psi$  terms are not considered. We confirmed  
389 that the exclusion of  $4\psi$  terms does not affect the results of  $2\psi$  terms.

390 In this study, both the isotropic and anisotropic terms of phase speed perturba-  
391 tions are expanded in spherical B-spline functions as for the case of the isotropic  
392 inversion described in section 4. We employ a grid interval of 4 degrees for ex-  
393 panding both isotropic and anisotropic terms, so that we are able to retrieve reli-  
394 able and stable estimate of azimuthal variations of Rayleigh wave phase velocity  
395 in this region.

396 Figure 14 displays the obtained  $2\psi$  anisotropic terms plotted over the isotropic

397 phase velocity map for periods of 45 s, 70 s and 100 s, with each bar representing  
398 the direction of the fastest velocity at a given location. This figure shows that the  
399 fast phase velocity directions near the Pacific plate are subparallel to the Kuril and  
400 Japan Trenches at all the periods, indicating the influence of the subducting Pa-  
401 cific plate on the azimuthal anisotropy in this region. A similar pattern of seismic  
402 anisotropy has been observed in several major subduction systems from the obser-  
403 vations of shear wave splitting, probably caused by significant trench parallel flow  
404 (Anderson et al., 2004; Nakajima and Hasegawa, 2004; Kneller and van Keken,  
405 2007; Wang and Zhao, 2008, 2009).

406 In contrast, the azimuthal anisotropy is weak beneath the Seas of Okhotsk and  
407 Japan. The back-arc spreadings of these marginal seas ceased about 10 Ma, and  
408 currently inactive, implying no vigorous geodynamic activities at present.

## 409 **7. Conclusions**

410 The three-stage surface wave tomography was successfully applied to the  
411 IRIS-FARM data in the northeastern Eurasian region and the temporary broad-  
412 band seismic network in Far Eastern Russia, including effects of off-great circle  
413 propagation and finite frequency. The fundamental and first two higher modes of  
414 Rayleigh waves in a period range from 30 to 150 s were inverted for a S-wave  
415 velocity model for each pair of source and station. The available data set allowed  
416 us to resolve the structure beneath the Japanese Islands and the Seas of Japan and  
417 Okhotsk down to 200 km depth with the average lateral resolution of 5 degrees.

418 Our final three-dimensional S-wave velocity model revealed a high velocity  
419 anomaly along the subduction zones, which is associated with the subducting Pa-  
420 cific plate. The velocity differences between the slabs and the surrounding mantle

421 reaches 6 percents. The mantle wedge is imaged as a low velocity zone, adjacent  
422 to each part of the subducting plate. In the southern Sea of Okhotsk, S-wave ve-  
423 locity reaches 4 km/s in the depth range of 80-160 km. This low velocity anomaly  
424 can be interpreted as mantle wedge of thermal anomalies with possible partial melt  
425 in the upper mantle. Our result seems to support a hypothesis of hot upwelling  
426 flow in the mantle in this area.

427 A large-scale high velocity anomaly of at least 500 km wide is detected in  
428 the northwestern Sea of Okhotsk, that is, in the north of the subducting slab and  
429 the above mantle wedge. This high velocity anomaly of 6 percent is extended  
430 subparallel to the present Pacific subduction zone. We interpret this anomaly to  
431 be a relict of the subducted Okhotsk plate, as suggested by Gorbatov et al. (2000).  
432 The lithosphere of the northern part is slightly faster than the other parts in the Sea  
433 of Japan, consistent with the result of a recent study by Yoshizawa et al. (2010).

434 The azimuthal anisotropy estimated from the phase velocity of the fundamen-  
435 tal mode Rayleigh waves revealed that the direction of anisotropic fast axis is  
436 oriented nearly parallel to adjacent trenches, reflecting strong influence of the  
437 presence of a subducting slab on the current mantle flow. The anisotropy beneath  
438 the marginal seas seems to be weak, where the present-day tectonic activity is less  
439 than the neighbouring subduction zones.

#### 440 **Acknowledgements**

441 We are grateful to the staff of the IRIS Data Management Center, the broad-  
442 band seismic network in Far Eastern Russia, the Institute of Seismology and Vol-  
443 canology of Hokkaido University and the Data Center of IFREE/JAMSTEC for  
444 providing us with data. We wish to thank D. Zhao and an anonymous reviewer for

445 their helpful and constructive reviews. The first author (EB) was supported during  
446 the main period of this study by the Research Fellowship from the Japan Society  
447 of Promotion of Science. This study was partly supported by a Grant-in-Aid for  
448 Scientific Research (No. 16075201, 17740283) from the Ministry of Education,  
449 Culture, Sports, Science and Technology of Japan. The GMT software package  
450 was used to plot the figures in this paper.

- 451 Anderson, M. L., Zandt, G., Triep, E., Fouch, M., Beck, S, 2004. Anisotropy and  
452 mantle flow in the Chile-Argentina subduction zone from shear wave splitting  
453 analysis. *Geophys. Res. Lett.* 31, doi:10.1029/2004GL020906.
- 454 Ando, M., 1975. Source mechanisms and tectonic significance of historical earth-  
455 quakes along the nankai trough, Japan. *Tectonophys.* 27, 2, 119-140.
- 456 Backus, G.E., 1965. Possible forms of seismic anisotropy of the uppermost mantle  
457 under oceans. *J. Geophys. Res.* 70, 14, 3429-3439.
- 458 Bird, P., 2003. An updated digital model of plate boundaries. *Geochem. Geophys.*  
459 *Geophys.* 4(3), 1027, doi:10.1029/2001GC000252.
- 460 Cara, M., L ev eque, J.J., 1987. Waveform inversion using secondary observables.  
461 *Geophys. Res. Lett.* 14, 1046 1049.
- 462 Castle, J. C., Creager, K. C., 1998. NW Pacific slab rheology, the seismicity cutoff,  
463 and the olivine to spinel phase change. *Earth Planets Space* 50, 977985.
- 464 Dahlen, F. A., Tromp, J., 1998. *Theoretical Global Seismology*, Princeton Univ.  
465 Press, Princeton, N. J.
- 466 DeMets, C., 1992. Oblique convergence and deformation along the Kuril and  
467 Japan trenches. *J. Geophys. Res.* 97, 17615-17626.
- 468 DeMets, C., Gordon R. G., Argus, D. F., Stein, S., 1990. Current plate motions.  
469 *Geophys. J. Int.* 101, 425-478.
- 470 Dziewonski, A.M., Anderson, D.L., 1981. Preliminary reference Earth model.  
471 *Phys. Earth Planet. Inter.* 25, 297-356.

- 472 Ekström, G., Dziewonski, A.M., Maternovskaya, N.N., Nettles, M., 2005. Global  
473 seismicity of 2003: centroidmoment-tensor solutions for 1087 earthquakes.  
474 Phys. Earth Planet. Inter. 148, 327-351.
- 475 Fukao, Y., Widiyantoro, R.D., Ohbayashi, M., 2001. Stagnant slab in the upper  
476 and lower mantle transition zone. Rev. Geophys. 39, 291-323.
- 477 Gorbatov, A., Kostoglodov, V., Suarez, G., Gordeev, E., 1997. Seismicity and  
478 structure of the Kamchatka subduction zone. J. Geophys. Res. 102, 17883-  
479 17898.
- 480 Gorbatov, Widiyantoro, S., Fukao, Y., Gordeev, E., 2000. Signature of remnant  
481 slabs in the North Pacific from P-wave tomography. Geophys. J. Int. 142, 27-  
482 36.
- 483 Hasegawa, A., Horiuchi, S., Umino, N., 1994. Seismic structure of the northeast-  
484 ern Japan convergent margin: A synthesis. J. Geophys. Res. 99, B11, 22295-  
485 22311.
- 486 Hasegawa, A., Umino, N., Takagi, A., 1978. Double-planed structure of the deep  
487 seismic zone in the northeastern Japan arc. Tectonophys. 47, 43-58.
- 488 Hasegawa, A., Zhao, D., Hori, S., Yamamoto, A., Horiuchi, S., 1991. Deep struc-  
489 ture of the northeastern Japan arc and its relationship to seismic and volcanic  
490 activity Nature 35, 683-689.
- 491 Huang, J., Zhao, D., 2006. High-resolution mantle tomography of China and sur-  
492 rounding regions. J. Geophys. Res. 111, B09305, doi:10.1029/2005JB004066.



- 493 Isse, T, Yoshizawa, K., Shiobara, H., Shinohara, M Nakahigashi, K., Mochizuki,  
494 K., Sugioka, H., Suetsugu,D., Oki, S., Kanazawa, K., Suyehiro, K., Fukao, Y.,  
495 2006. Three-dimensional shear wave structure beneath the Philippine Sea from  
496 land and ocean bottom broadband seismograms. *J. Geophys. Res.* 111, B06310,  
497 doi:10.1029/2005JB003750.
- 498 Katsumata, K., Wada, N., Kasahara, M., 2003. Newly imaged shape of the  
499 deep seismic zone within the subducting Pacific plate beneath the Hokkaido  
500 corner, Japan-Kurile arc-arc junction. *J. Geophys. Res.* 108, B12, 2565,  
501 doi:10.1029/2002JB002175.
- 502 Kennett, B.L.N., 1995. Approximations for surface-wave propagation in laterally  
503 varying media. *Geophys. J. Int.* 122, 2, 470-478.
- 504 Kennett, B.L.N., Yoshizawa, K., 2002. A reappraisal of regional surface wave  
505 tomography. *Geophys. J. Int.* 150, 1, 37-44.
- 506 Kimura, G., 1994. The latest Cretaceous - early Paleogene rapid growth of accre-  
507 tionary complex and exhumation of high pressure series metamorphic rocks in  
508 northwestern Pacific margin. *J. Geophys. Res.* 99, 22147-22164.
- 509 Kneller, E.A., van Keken, P.E., 2007. Trench-parallel flow and seismic  
510 anisotropy in the Mariana and Andean subduction systems. *Nature* 450,  
511 doi:10.1038/nature06429.
- 512 Lancaster, P., Salkauskas, K., 1986. *Curve and Surface Fitting*. Academic, San  
513 Diego, Calif.
- 514 Lebedev, S., Nolet, G., 2003. Upper mantle beneath Southeast Asia from S veloc-  
515 ity tomography. *J. Geophys. Res.* 108, B1, 2048, doi:10.1029/2000JB000073.

- 516 Lei, J., Zhao, D., 2005. P-wave tomography and origin of the Changbai intraplate  
517 volcano in Northeast Asia. *Tectonophys.* 397, 281-295.
- 518 Li H.-Y., Liu, F.-T., Sun, R.-M., Zheng, Y.-J., Peng, Y.-J., Huang, Z.-X., 2001.  
519 Crust and upper mantle structure in east China and sea areas. *Acta Seismologica*  
520 *Sinica*, 14, 5, 503-511.
- 521 Miller, M.S., Kennett, B.L.N., Toy, V.G., 2006. Spatial and temporal evolution  
522 of the subducting Pacific plate structure along the western Pacific margin. *J.*  
523 *Geophys. Res.* 111, B02401, doi:10.1029/2005JB003705.
- 524 Mishra, O.P., Zhao, D., Umino, N., Hasegawa, A., 2003. Tomography of northeast  
525 Japan forearc and its implications for interplate seismic coupling. *Geophys.*  
526 *Res. Lett.* 30, 16, 1850, doi:10.1029/2003GL017736.
- 527 Miyamachi, H., Ichiyanagi, M., Maeda, T., Yamaguchi, T., Takada, M., Takahashi,  
528 H., Kasahara, M., Hirano, S., Sen Rak Se, Mikhaylov V., Mikrukoba, O., Levin,  
529 Yu., Kim Chun Ung, Vasilenko, N., Shestakov, N., Gerasimeko, M., Bormotov  
530 V., Luneva M., Gunbina L., 2009. Construction of the broadband seismic net-  
531 work in Far Eastern Russia for imaging the stagnant slab. *Geophysical Bulletin*  
532 *of Hokkaido University* 72, 37-49.
- 533 Nakajima, J., Hasegawa, A., 2004. Shear-wave polarization anisotropy and  
534 subduction-induced flow in the mantle wedge of northeastern Japan. *Earth*  
535 *Planet. Sci. Lett.* 225, 365-377.
- 536 Nataf, H.-C., and Y. Ricard, 1996. 3SMAC: An a priori tomographic model of  
537 the upper mantle based on geophysical modeling. *Phys. Earth Planet. Inter.* 95,  
538 101122.

539 Nataf, H.C., Nakanishi, I., Anderson, D.L., 1986. Measurements of numerous  
540 useful discussions. We also wish to thank the members of RSES mantle wave  
541 velocities and inversion for lateral heterogeneities and at the Australian Na-  
542 tional University for their invaluable support for anisotropy: 3. Inversion. *J.*  
543 *Geophys. Res.* 91, 72617307.

544 Nishimura, C. E., Forsyth, D., W., 1989. The anisotropic structure of the upper  
545 mantle in the Pacific. *Geophys. J.* 96, 203–229.

546 Parfenov, L.M., Natal'in, B.A., 1985. Mesozoic accretion and collision tectonics  
547 of northeastern Asia, in *Tectonostratigraphic Terranes of the Circum-Pacific*  
548 *Region*, pp. 363–373, ed. Howell, D.G., Circum-Pacific Council, Houston, TX.

549 Park, J., Levin, V., Lees, J., Brandon, M.T., Peyton, V., Gordeev, E., Ozerov, A.,  
550 2002. Seismic anisotropy and mantle flow in the Kamchatka-Aleutian corner,  
551 In: S. Stein (ed), *Plate Boundary Zones*, Geophysical Monograph, American  
552 Geophysical Union, Washington DC.

553 Priestley, K., Debayle, E., McKenzie, D., Pilidou, S., 2006. Upper mantle struc-  
554 ture of eastern Asia from multimode surface waveform tomography. *J. Geo-*  
555 *phys. Res.* 111, B10304, doi:10.1029/2005JB004082.

556 Ritzwoller, M.H., Levshin, A.L., 1998. Eurasian surface wave tomography:  
557 Group velocities. *J. Geophys. Res.* 103, B3, 4839–4878.

558 Sambridge, M., 1999. Geophysical inversion with a Neighbourhood algorithm I.  
559 Searching a parameter space. *Geophys. J. Int.* 138, 479–494.

560 Seno, T., 1999. Syntheses of the regional stress fields of the Japanese islands. *The*  
561 *Island Arc* 8, 1, 66–79.

- 562 Seno, T., Sakurai, T., Stein, S., 1996. Can the Okhotsk plate be discriminated from  
563 the North American plate? *J. Geophys. Res.* 101, 11305-11315.
- 564 Seno, T., Stein, S., Gripp, A.E., 1993. A model for the motion of the Philippine  
565 Sea consistent with NUVEL-1. *J. Geophys. Res.* 98, 17941-17948.
- 566 Shelly, D.R., Beroza, G.C., Zhang, H., Thurber, C.H., Ide, S., 2006. High-  
567 resolution subduction zone seismicity and velocity structure beneath Ibaraki  
568 Prefecture, Japan. *J. Geophys. Res.* 111, B06311, doi:10.1029/2005JB004081
- 569 Smith, M. L., Dahlen, F.A., 1973. The Azimuthal Dependence of Love and  
570 Rayleigh Wave Propagation in a Slightly Anisotropic Medium. *J. Geophys. Res.*  
571 78, 17, 3321-3333.
- 572 Sugimura, A., 1972. Plate boundaries near Japan. *Kagaku (Sci.)*, 42, 192-202 (in  
573 Japanese).
- 574 Taira, A., 2001. Tectonic evolution of the Japanese islands arc system. *Annu. Rev.*  
575 *Planet. Sci.* 29, 109-134.
- 576 Takeuchi, H., and M. Saito (1972), Seismic surface waves, in *Seismology: Surface*  
577 *Waves and Free Oscillations, Methods Comput. Phys.*, vol. 11, edited by B. A.  
578 Bolt, pp. 217-295, Academic, San Diego, Calif.
- 579 Tarantola, A., Valette, B., 1982. Generalized nonlinear inverse problems solved  
580 using the least-squares criterion, *Rev. Geophys.* 20, 219-232.
- 581 Takezoe, H., Yoshizawa, K., Yomogida, K., 2005. Rayleigh wave phase velocity  
582 distribution in the Japanese islands estimated from array analysis, *Proc. Symp.*  
583 *Stagnant Slab Project*, 70-72. (in Japanese)

- 584 van der Hilst, R. D., Engdahl, E. R., Spakman, W., Nolet, G., 1991, Tomographic  
585 imaging of subducted lithosphere below northwest Pacific island arcs. *Nature*  
586 353, 3743.
- 587 van der Hilst, R. D., Widiyantoro, S., Creager, K.C., McSweeney, T. J., 1998.  
588 Deep subduction and aspherical variations in P-wavespeed at the base of Earth's  
589 mantle, *Geodynamics*, AGU 28 520.
- 590 van Heijst, H.J., Woodhouse, J., 1999. Global high resolution phase velocity  
591 distributions of overtone and fundamental-mode surface waves determined by  
592 mode branch stripping. *Geophys. J. Int.* 137, 601-620.
- 593 Verzhbitsky, E.V., Berlin, Yu.M., Kononov, M.V., Marina, M.M., 2006. Esti-  
594 mates of the temperatures of hydrocarbon generation in the region of the Sea of  
595 Okhotsk. *Oceanology* 46, 4, 572-583.
- 596 Verzhbitsky, E.V., Kononov, M.V., 2006. Geodynamic evolution of the lithosphere  
597 of the Sea of Okhotsk region from geophysical data. *Izvestiya Physics of the*  
598 *Solid Earth* 42, 6, 490-501.
- 599 Wang, Z., Dahlen, F.A., 1995. Spherical-spline parameterization of three-  
600 dimensional Earth models. *Geophys. Res. Lett.* 22, 30993102.
- 601 Wang, K., Zhao, D., 2005. Seismic imaging of the entire arc of Tohoku and  
602 Hokkaido in Japan using P-wave, S-wave and sP depth-phase data. *Phys. Earth*  
603 *Planet. Inter.* 152, 3, 144-162.
- 604 Wang, J., Zhao, D., 2008. P-wave anisotropic tomography beneath Northeast  
605 Japan *Phys. Earth Planet. Inter.* 170, 115-133.

- 606 Wang, J., Zhao, D., 2009. P-wave anisotropic tomography of the crust and upper  
607 mantle under Hokkaido, Japan. *Tectonophysics* 469, 137-149.
- 608 Wei, D., Seno, T., 1998. Determination of the Amurian plate motion, in *Mantle*  
609 *Dynamics and Plate Interactions in East Asia*, Geodyn. Ser. 27, edited by M. F.  
610 J. Flower et al., 419 p., AGU, Washington, DC.
- 611 Widiyantoro, S., Kennett, B.L.N., van der Hilst, R.D., 1999. Seismic tomography  
612 with P and S data reveals lateral variations in the rigidity of deep slabs. *Earth*  
613 *Planet. Sci. Lett.* 173, 91100.
- 614 Yoshizawa, K., Ekström, G., 2009. Automated multi-mode phase speed mea-  
615 surements for high-resolution regional-scale tomography: Application to North  
616 America. *Geophys. J. Int.* submitted.
- 617 Yoshizawa, K., Kennett, B.L.N., 2002a. Non-linear waveform inversion for sur-  
618 face waves with a neighbourhood algorithm-application to multimode disper-  
619 sion measurements. *Geophys. J. Int.* 149, 1, 118-133.
- 620 Yoshizawa, K., Kennett, B.L.N., 2002b. Determination of the influence zone for  
621 surface wave paths. *Geophys. J. Int.* 149, 440453.
- 622 Yoshizawa, K., Kennett, B.L.N., 2004. Multimode surface wave tomography for  
623 the Australian region using a three-stage approach incorporating finite fre-  
624 quency effects. *J. Geophys. Res.* 109, B02310, doi:10.1029/2002JB002254.
- 625 Yoshizawa, K., Miyake, K., and Yomogida, K., 2010. 3-D upper man-  
626 tle structure beneath Japan and its surround region from inter-station  
627 dispersion measurements of surface waves, *Phys. Earth Planet. Inter.*  
628 doi:10.1016/j.pepi.2010.02.012.

- 629 Zhao, D., 2001. New advances of seismic tomography and its applications to sub-  
630 duction zones and earthquake fault zone: A review. *The Island Arc* 10, 68-84.
- 631 Zhao, D., 2004. Global tomographic images of mantle plumes and subducting  
632 slabs: insight into deep Earth dynamics. *Phys. Earth Planet. Inter.* 146, 334.
- 633 Zhao, D., 2009. Multiscale seismic tomography and mantle dynamics. *Gondwana*  
634 *Research* 15, 297323.
- 635 Zhao, D., Hasegawa, A., Kanamori, H., 1994. Deep structure of Japan subduction  
636 zone as derived from local, regional, and teleseismic events. *J. Geophys. Res.*  
637 99, 22313-22329.
- 638 Zhao, D., Wang, Z., Umino, N., Hasegawa, A., 2009. Mapping the mantle wedge  
639 and intraplate thrust zone of the northeast Japan arc. *Tectonophysics* 467, 89-  
640 106.
- 641 Zonenshain, L.P., Savostin, L.A., 1981. Geodynamics of the Baikal rift zone and  
642 plate tectonics of Asia. *Tectonophysics.* 76, 1-45.

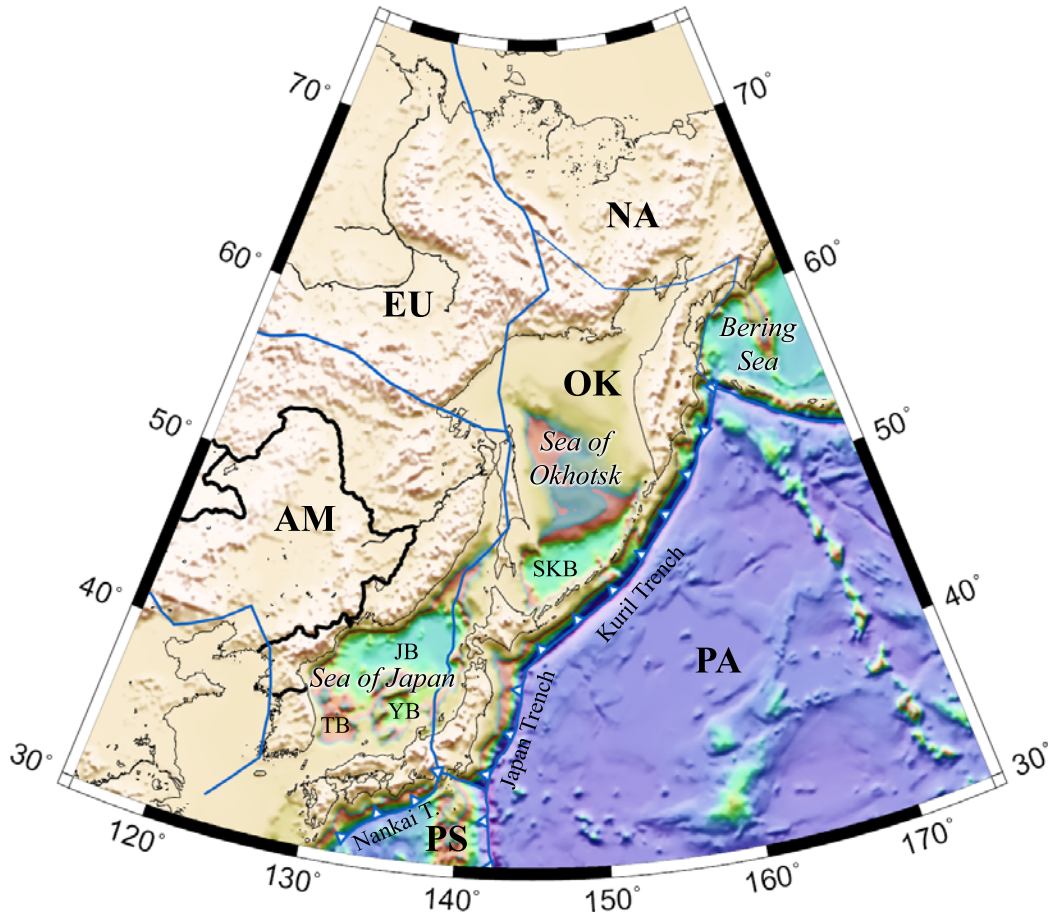


Figure 1: Tectonic map of the northeastern Eurasian region. Plate boundaries are indicated by solid lines according to PB2002 model by Bird (2003). PA: Pacific plate, PS: Philippine Sea plate, OK: Okhotsk plate, AM: Amur plate, NA: North American plate, EU: Eurasian plate. JB: Japan basin, YB: Yamato basin, TB: Tsushima basin, SKB: South Kuril basin.



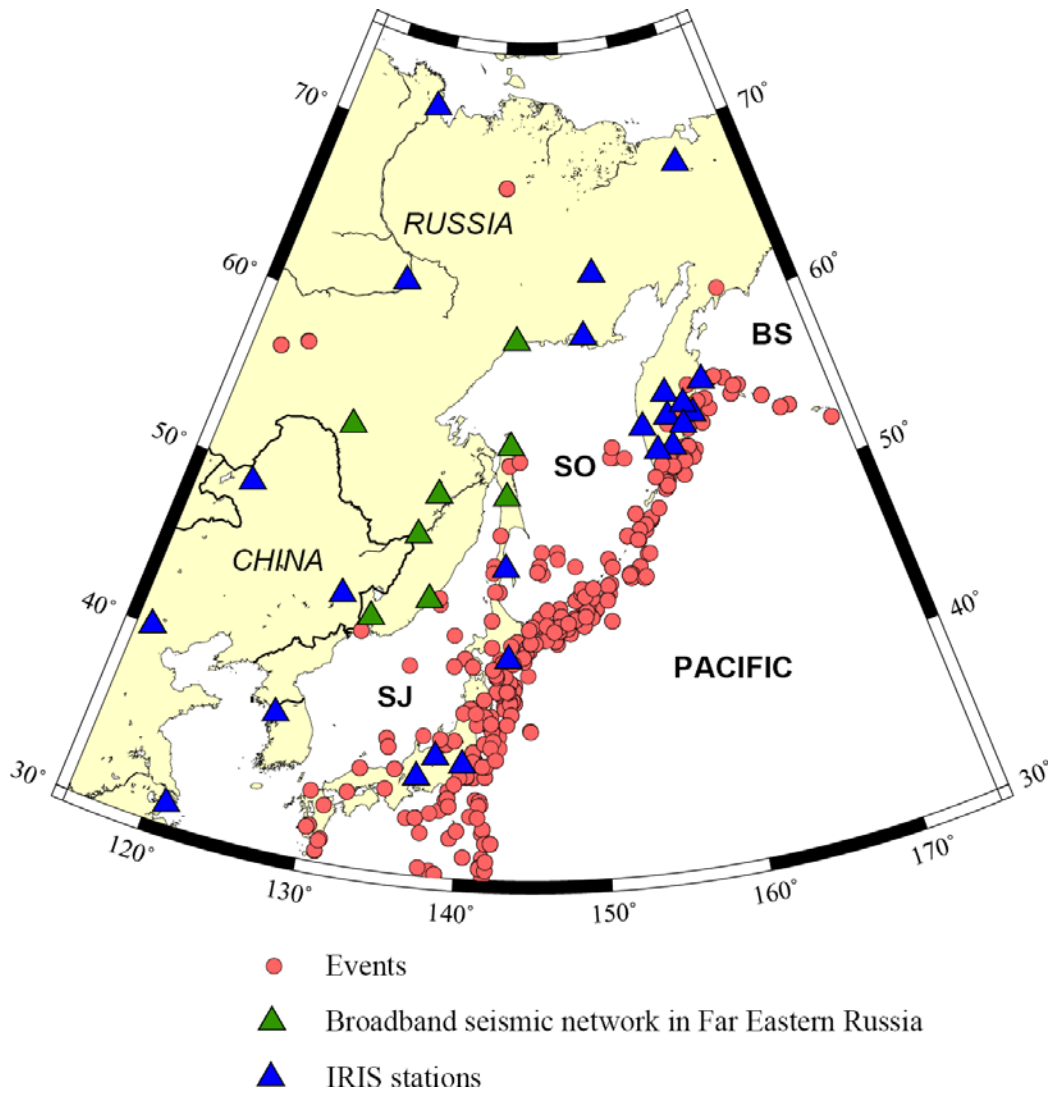


Figure 2: Events and station distributions of this study. The data set is composed of three-component seismograms recorded by 25 IRIS stations (blue triangles) and 8 stations of the broadband seismic network in Far Eastern Russia (green triangles) from 305 events (red circles). SJ: Sea of Japan, SO: Sea of Okhotsk, BS: Bering Sea.

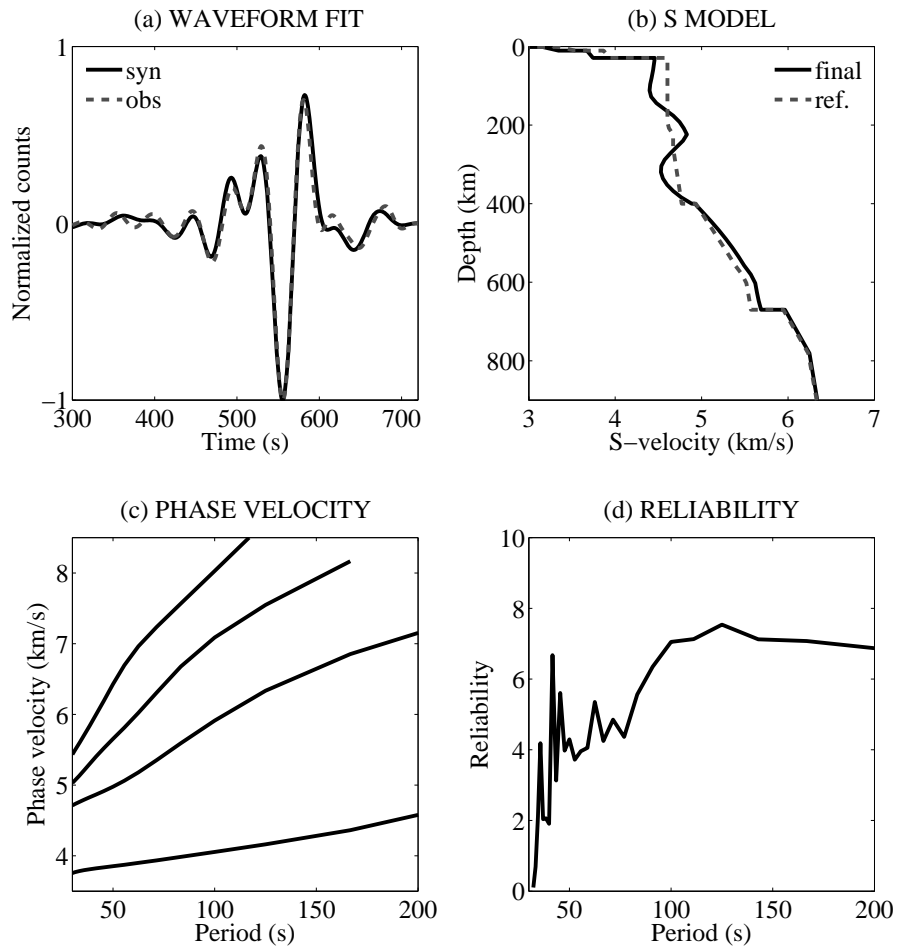


Figure 3: An example of NA waveform inversion for Rayleigh wave at the station HIA: (a) waveform fit; (b) path-average 1D profile; (c) multimode phase velocity dispersion curves estimated from this 1D model; (d) reliability parameter.

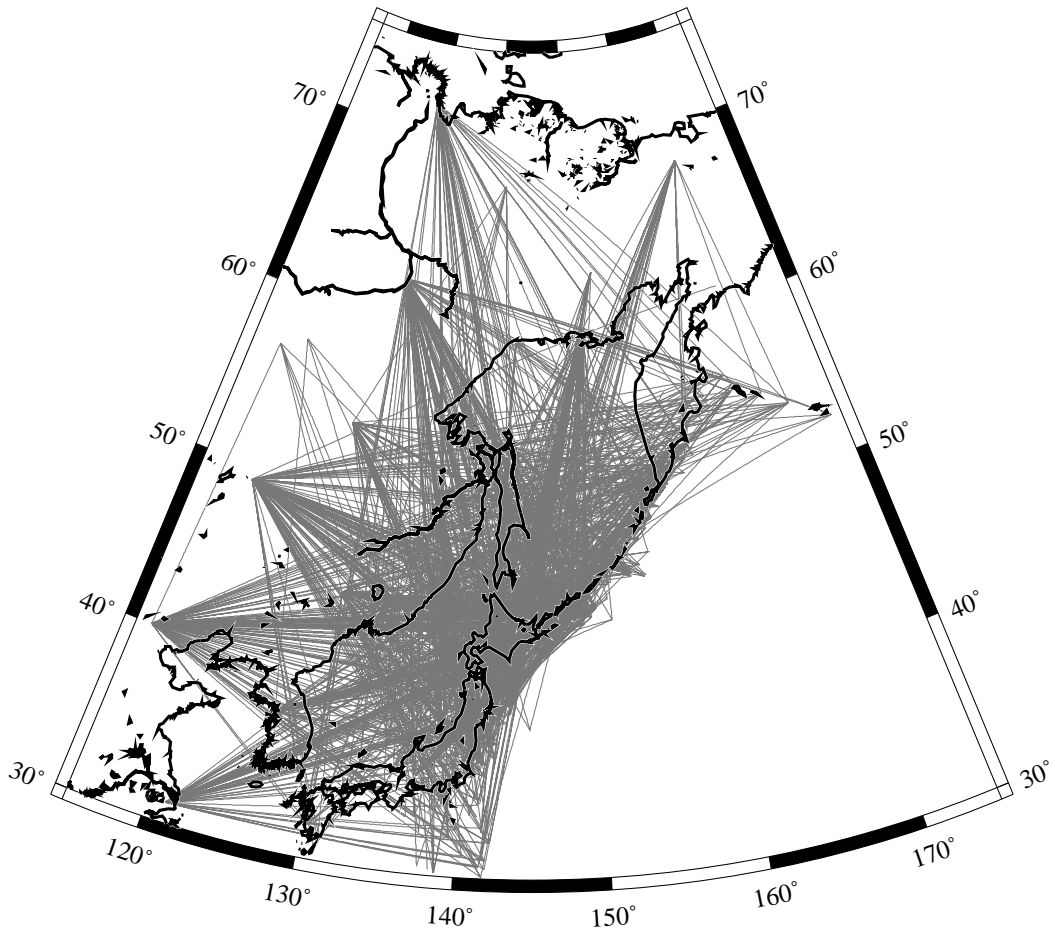


Figure 4: Distribution of the total number of 1129 paths used to constrain phase velocity models. The number of used paths for each phase velocity model depends on period and mode, varying from 980 to 1099 with all the paths displayed in this Figure.

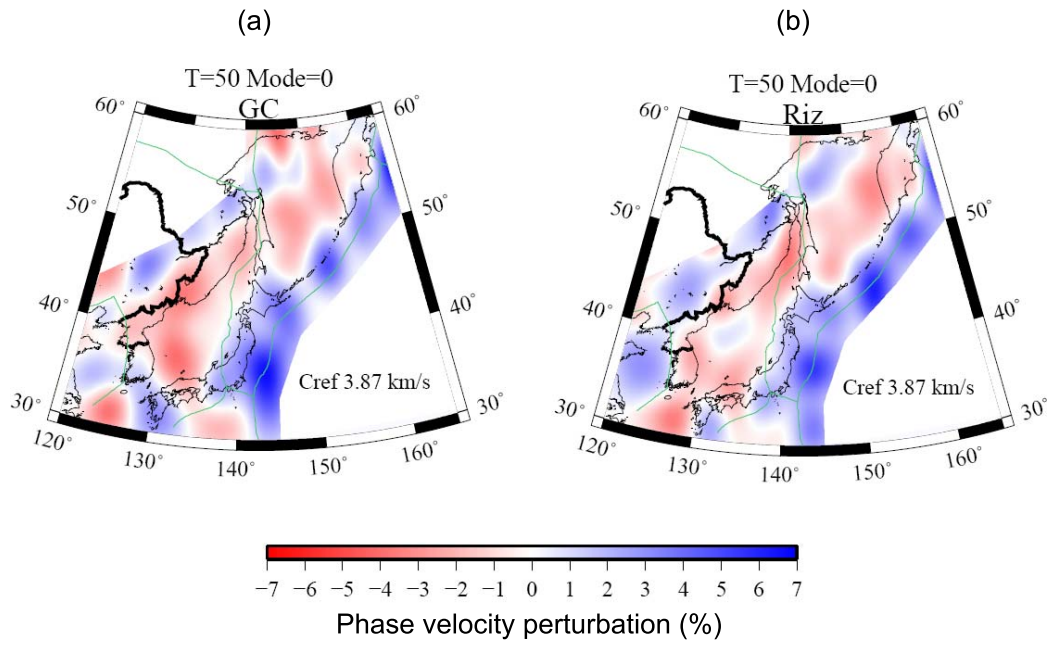


Figure 5: Phase velocity perturbation maps of the fundamental mode Rayleigh wave at 50 s period obtained for (a) the GC model and (b) Riz model. The reference phase velocity is 3.87 km/s.

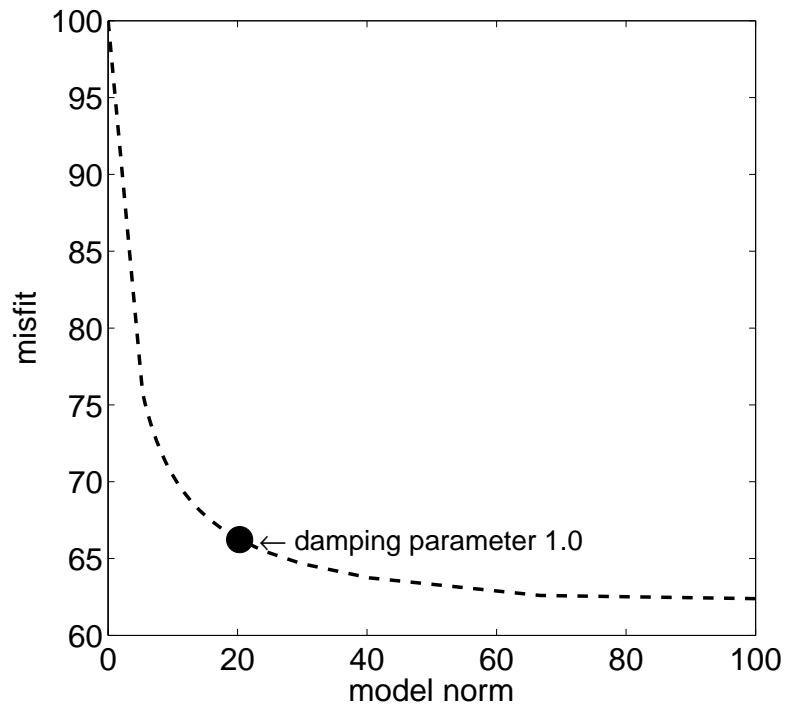


Figure 6: Trade-off curve between the misfit and the model norm for different damping parameters in the Riz model at period of 100 s. We chose the damping parameter  $\lambda = 1.0$  as the most appropriate for this inversion.

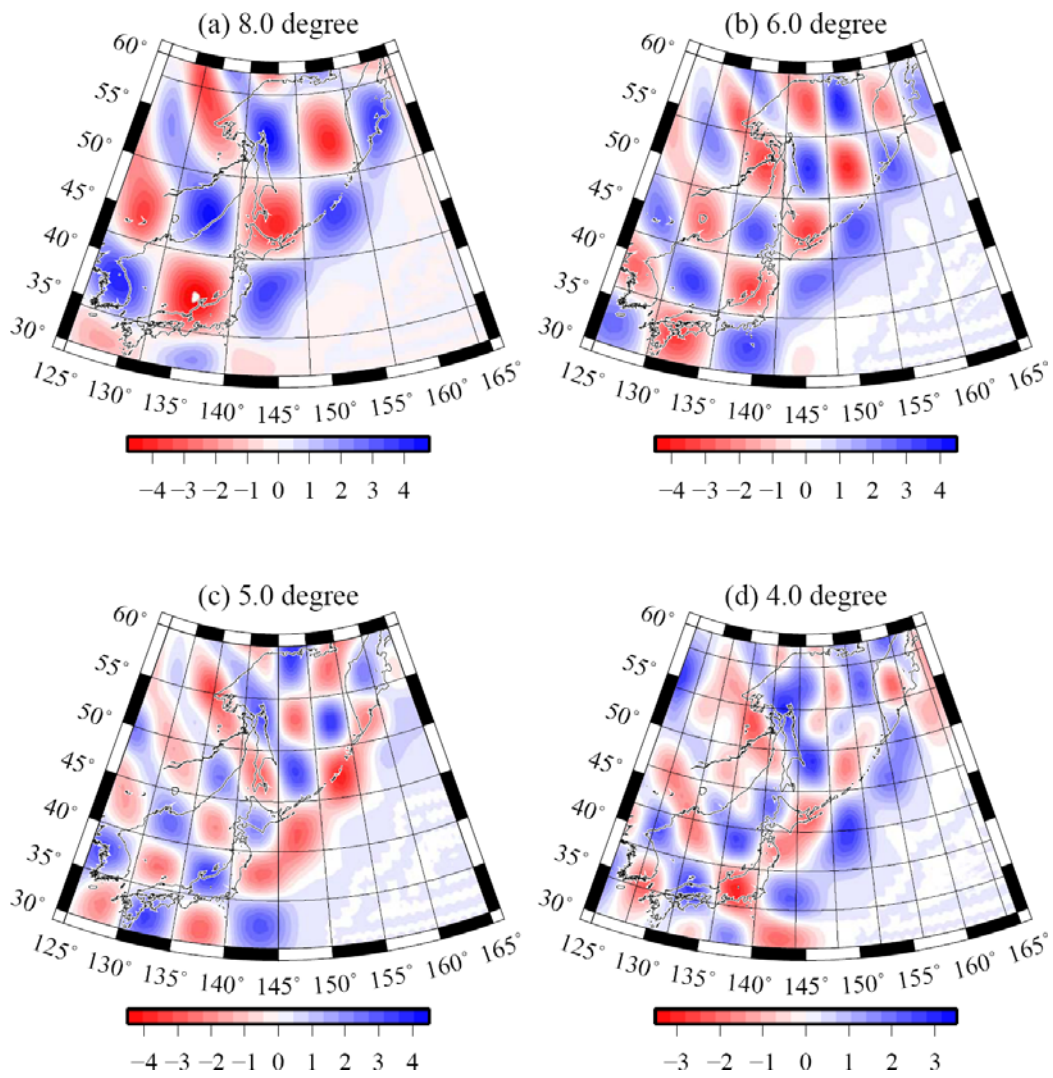


Figure 7: Results of checkerboard resolution tests at period of 50 s for different cell sizes: 8, 6, 5 and 4 degrees.

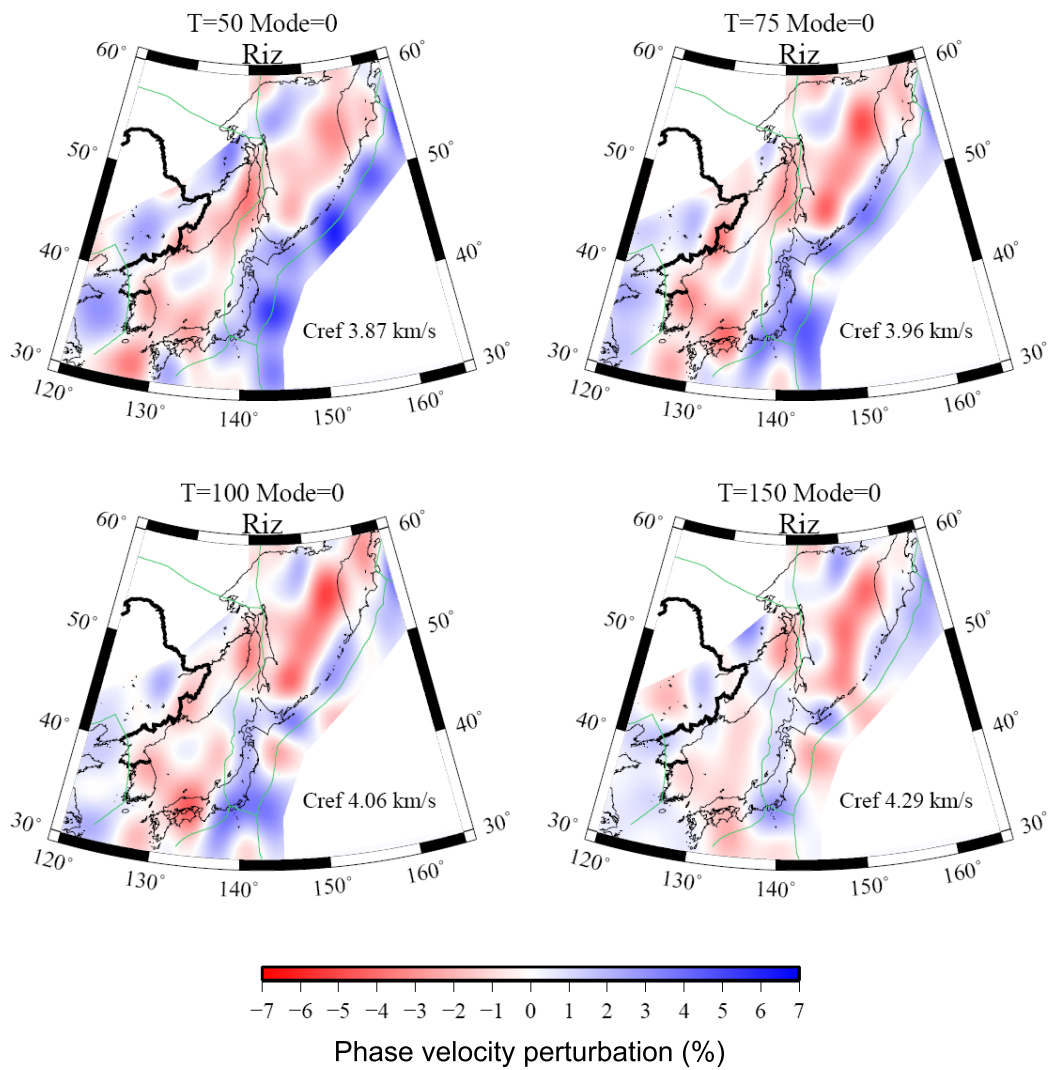


Figure 8: Phase velocity maps of the fundamental mode Rayleigh waves obtained with 3 degree grid.

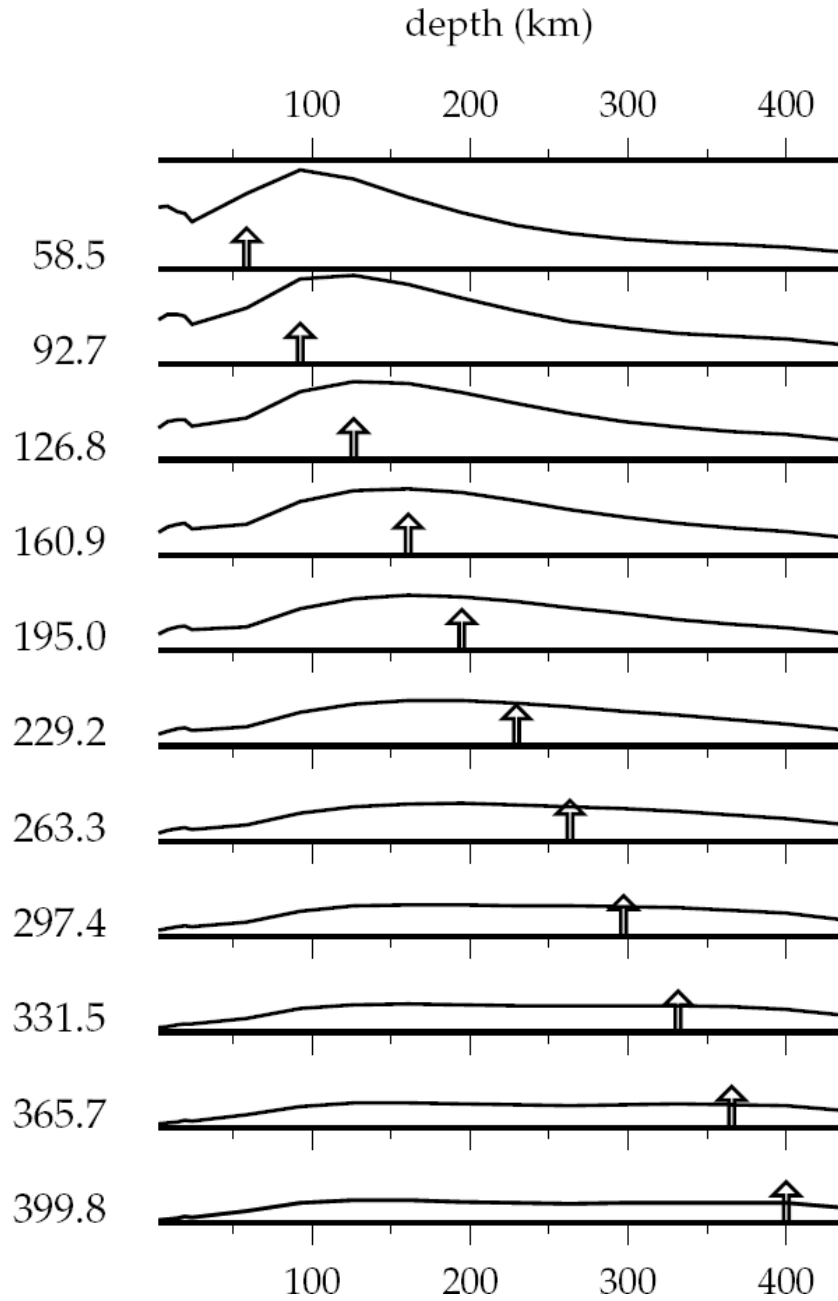


Figure 9: Resolution kernels for S-wave velocity profile beneath the location at (35°N, 140°E). An ideal vertical resolution would show a delta-like peak around each depth marked by arrows. In this example, the structure is relatively well resolved down to 200-250 km in depth, mainly due to the fundamental mode sensitivity.



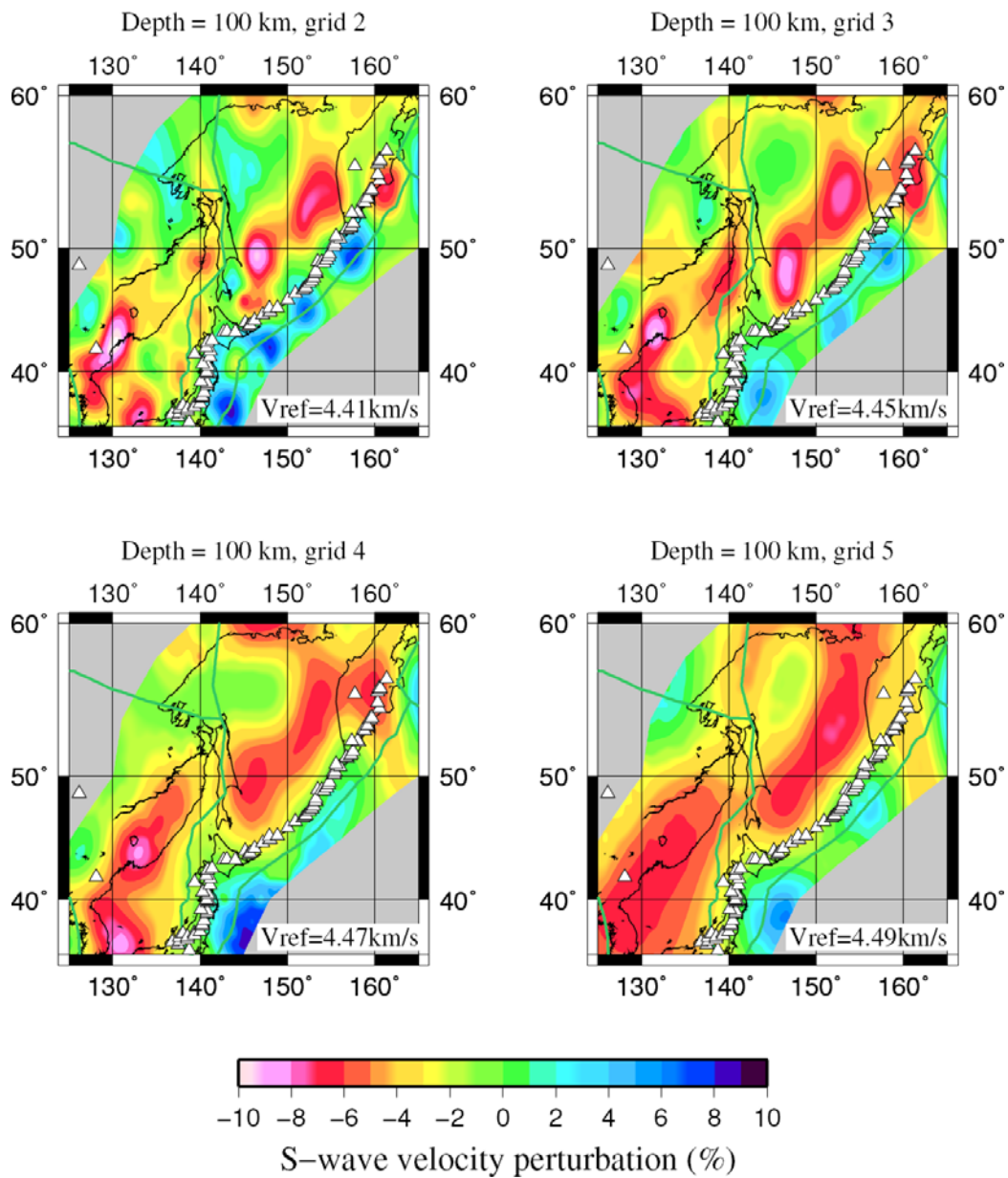


Figure 10: Comparison of S-wave velocity perturbation maps at 100 km depth with different grids: (a) 2, (b) 3, (c) 4 and (d) 5 degrees. The distribution of S-wave velocity in the region is plotted relative to the average S-wave velocity  $V_{ref}$  for each map. White triangles denote active volcanoes.

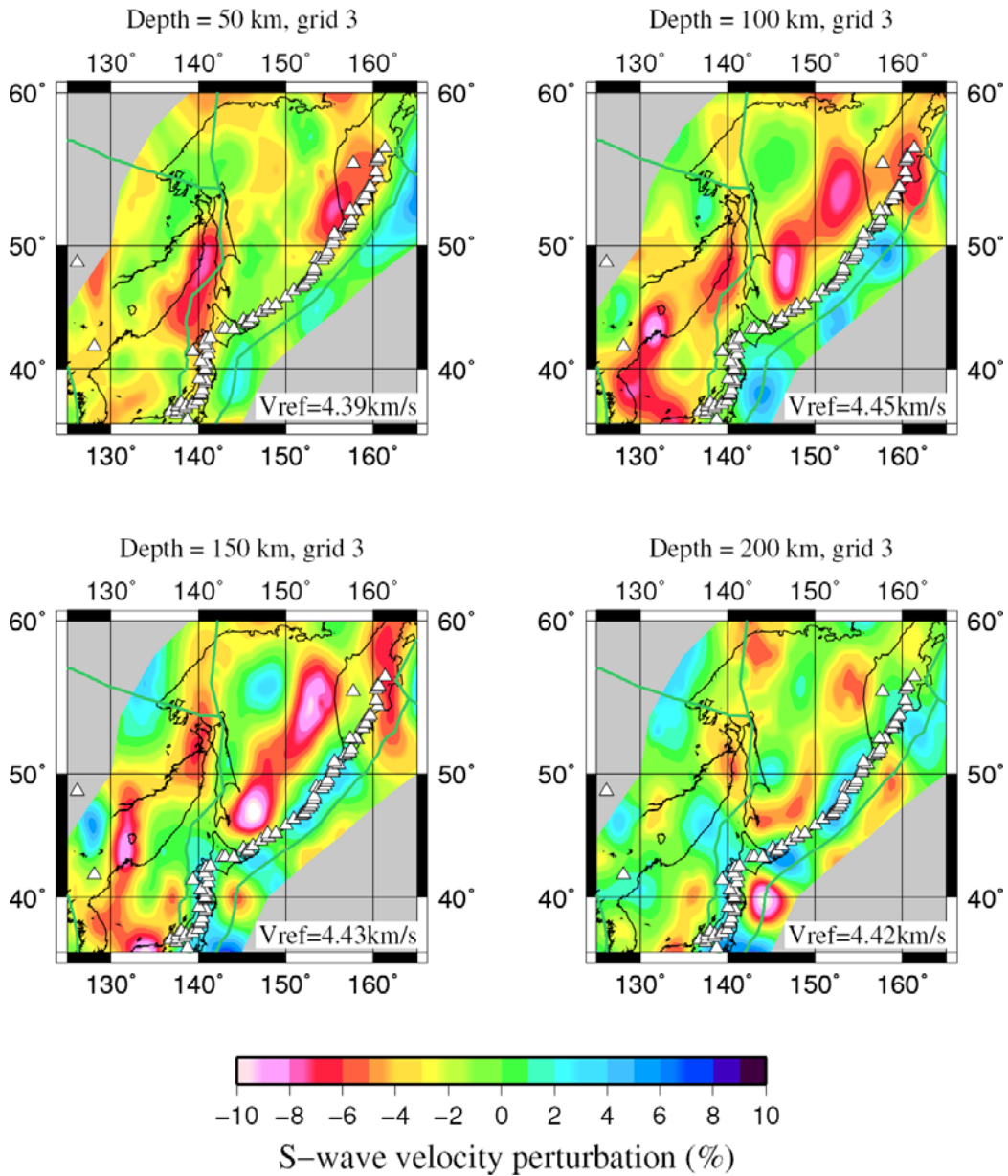


Figure 11: S-wave velocity perturbation maps for grids of 3 degrees from 50 to 200 km depth. The distribution of S-wave velocity in the region is plotted relative to the average S-wave velocity  $V_{ref}$  for each map. White triangles denote active volcanoes.

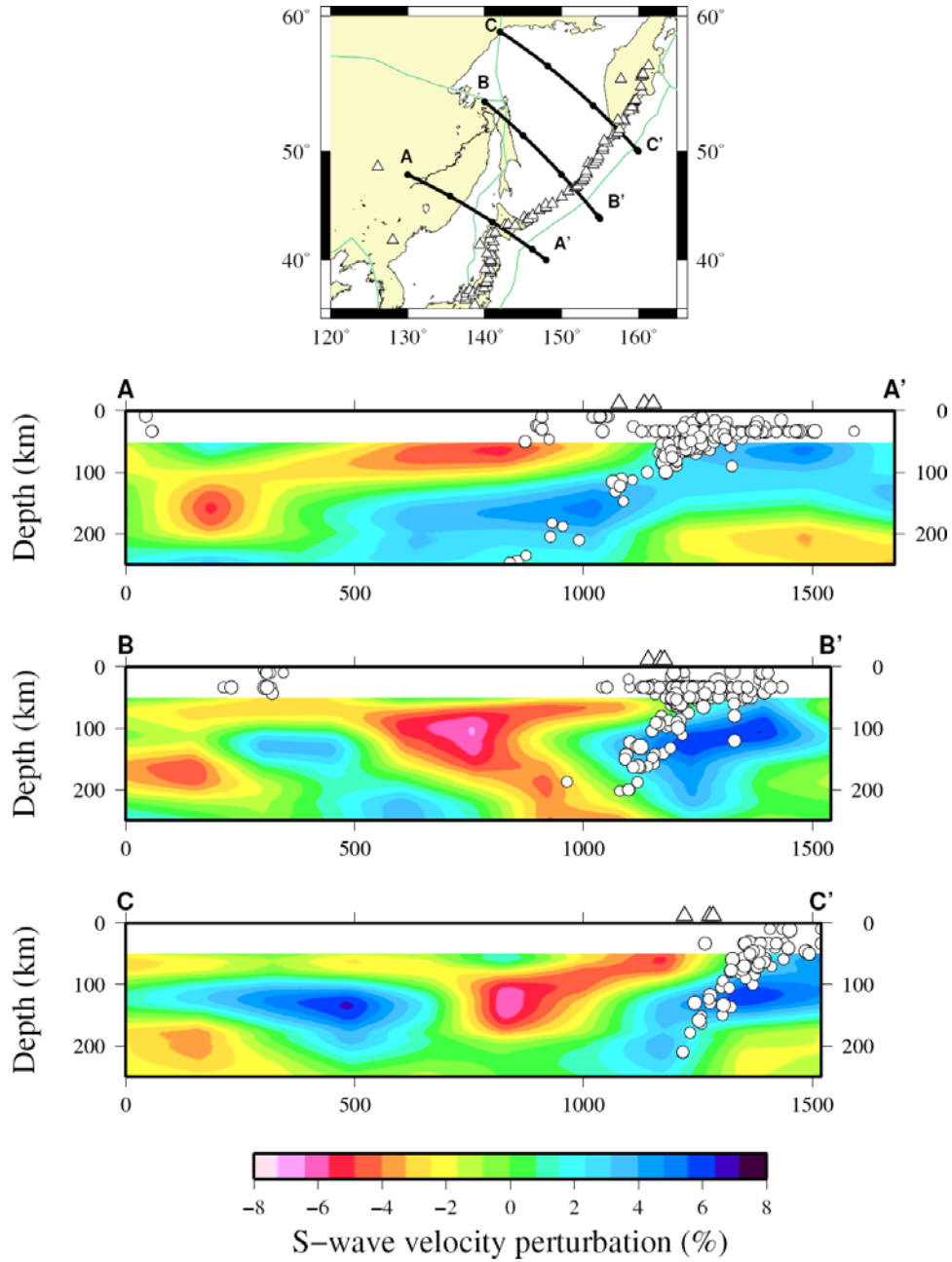


Figure 12: S-wave velocity cross sections along three profiles AA', BB' and CC'. The orientation of the profiles is perpendicular to each subduction trench axis. The distribution of S-wave velocity is plotted relative to the average S-wave velocity at each depth. White triangles denote active volcanoes. White circles show earthquakes that occurred along each profile.

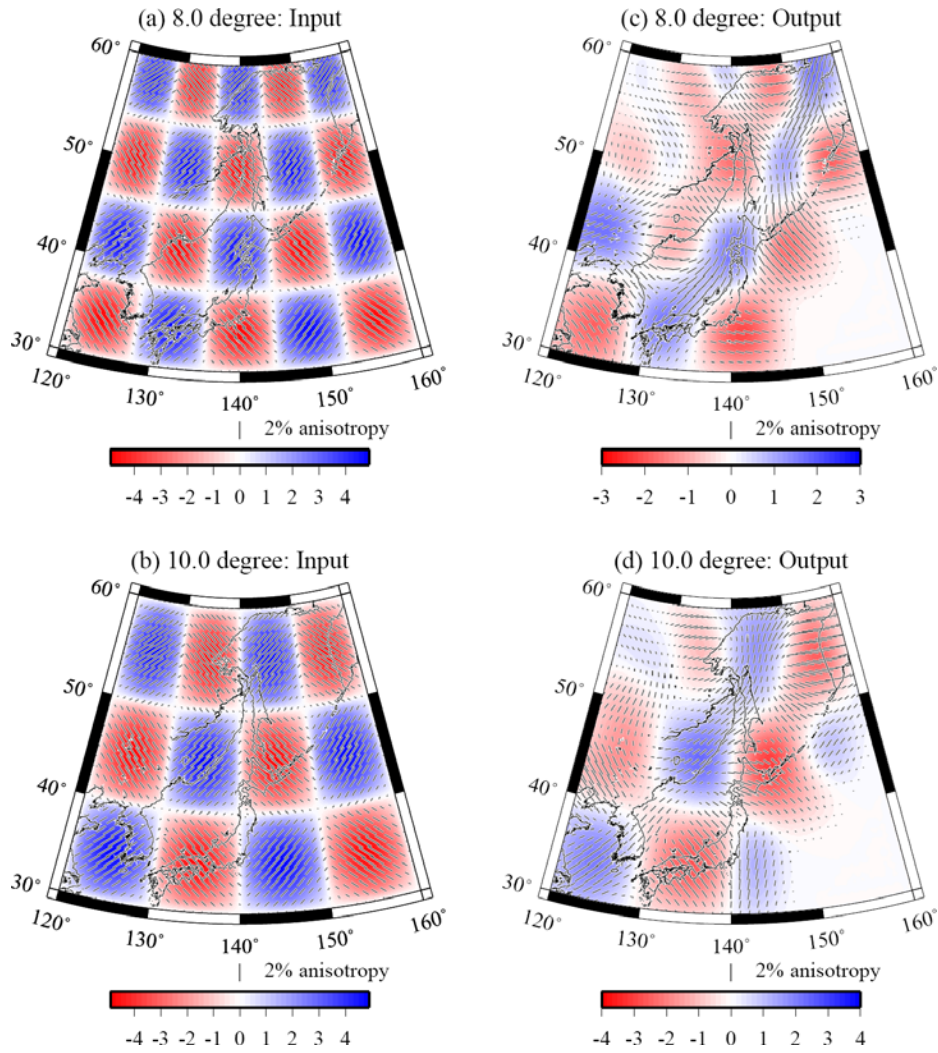


Figure 13: Results of checkerboard resolution test for azimuthal anisotropy at period of 50 s for 8 and 10-degree cellular patterns. (a,b) Input models for phase velocity with anomalies of  $\pm 4.8$ -percent amplitude and for the anisotropic term with 2% anisotropy at maximum. The fastest direction at each location is represented by the orientation of each bar, and the strength by its length. (c,d) Recovered isotropic heterogeneity and azimuthal anisotropy.

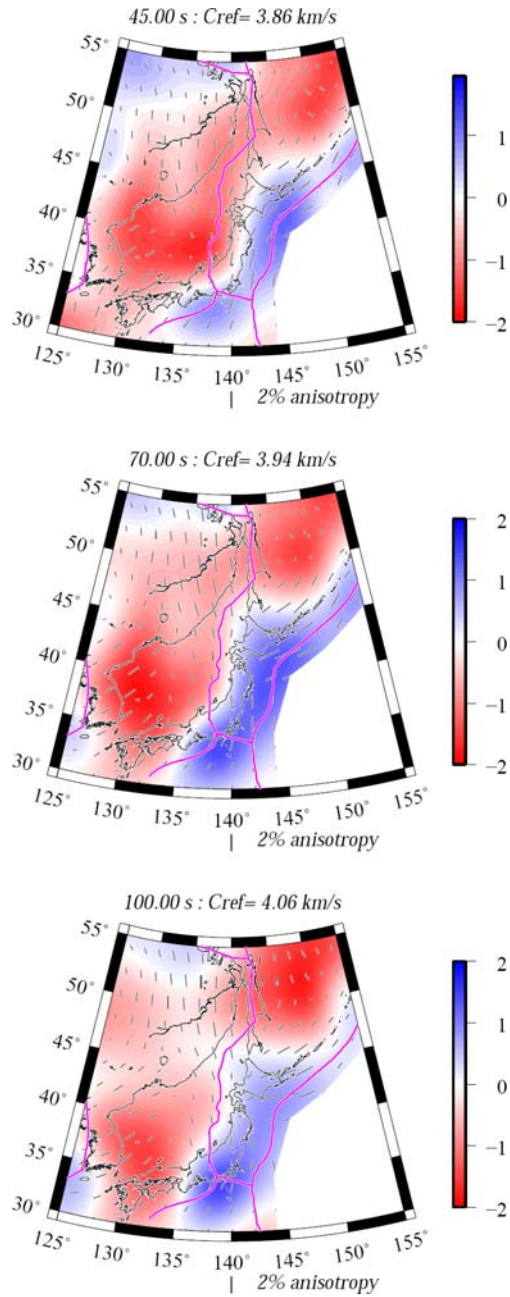


Figure 14: Phase velocity maps of the fundamental mode Rayleigh wave with anisotropic term at (a) 45 s, (b) 70 s and (c) 100 s. The fastest direction at each location is represented by the orientation of each bar, and the strength by its length.